Acta Geotechnica
DOI 10.1007/s11440-008-0060-5

RESEARCH PAPER

Earth curvature effects on subduction morphology: Modeling subduction in a spherical setting

Gabriele Morra · Philippe Chatelain · Paul Tackley · Petros Koumoutsakos

Received: 10 September 2007 / Accepted: 7 February 2008

Abstract We present the first application in geodynamics of a (Fast Multipole) Accelerated Boundary Element Method (Accelerated-BEM) for Stokes flow. The approach offers the advantages of a reduced number of computational elements and linear scaling with the problem size. We show that this numerical method can be fruitfully applied for the simulation of several geodynamic systems at the planetary scale in spherical coordinates, and we suggest a general approach for modeling combined mantle convection and plate tectonics. The first part of the paper is devoted to the technical exposition of the new approach, while the second part focuses on the effect played by Earth curvature on the subduction of a very wide oceanic lithosphere ($W = 6{,}000$ km and $W = 9{,}000$ km), comparing the effects of two different planetary radii (ER = 6,371 km, 2ER = 2 × 6,371 km), corresponding to an "Earth-like" model (ER) and to a "flat Earth" one (2ER). The results show a distinct difference between the two models: while the slab on a "flat Earth" shows a slight undulation, the same subducting plate on the "Earth-like" setting presents a dual behavior characterized by concave curvature at the edges and by a folding with wavelength of the order of magnitude of 1,000 km at the center of the slab.

G. Morra (✉)
Geology Department, Roma Tre University, Rome, Italy
e-mail: gabriele.morra@erdw.ethz.ch

G. Morra · P. Tackley
Geophysical Fluid Dynamics, ETH Zurich, Switzerland

P. Chatelain · P. Koumoutsakos
Computational Science and Engineering Laboratory,
ETH Zurich, Switzerland

Keywords Boundary elements · Fast multipole · Fluid dynamics · Global geodynamics · Nazca plate · Pacific plate · Plate tectonics · Subduction

1 Introduction

Mantle geodynamics is the study of the planetary solid phase evolution at large time scales, typically $T > O(1\text{ Ma})$. When the differential temperature and mantle thickness results in a sufficiently high Rayleigh number the mantle naturally convects, as it usually happens in terrestrial planets. On Earth, however, this process is superposed to the unique way Earth regenerates its surface through the subduction into the mantle of its shallowest thin layer, called lithosphere ($h_{\text{litho}} = O(100\text{ km}) \ll h_{\text{mantle}} = O(3{,}000\text{ km})$), which is generated at mid-ocean ridges.

The driving force on tectonic plates is the pull of the highly viscous subducting slabs while the driving mechanism of mantle convection is the differential temperature between the core mantle boundary and the earth surface [3, 7, 8, 9]. The short term ($O(100\text{ Ma})$) expression of plate tectonics and the long term ($O(1\text{ Ga})$) cooling of the Earth are due to the combined forcing from the top and the bottom [26, 36, 42]. In this manuscript, we model the dynamics of the largest tectonics plates, neglecting the slower global mantle flow.

The distribution of Earth plates size follows a power law [2, 34] of 0.25, implying that plate tectonics is dominated by the largest plates. When strong inner heterogeneities are not present, plate size and therefore trench width must have a fundamental role in subduction and, as a consequence of the power law scaling, the widest trenches must control the global process. Observation shows that most of the trenches on Earth are

caused by the subduction of three plates: Pacific, Nazca and Indian. Their trenches are segmented in "arcs", whose total length is of the order of $O(10^4$ km), comparable to planetary size [20, 33]. Recent works have addressed the role of plate size in subduction [32, 35] and the role of the width of segmented arc [22, 24]. They concluded that the inner heterogeneities are mostly important for shaping each trench segment (up to 2,000 km), while very long trenches (over 4,000 km) interact strongly with the mantle and display a kinematics characterized by low trench retreat and fast subduction velocities. Earth curvature has a negligible effect on the morphology and kinematics of the single arc [24] but it has not yet been established whether it has an effect on the widest subduction zones, and what sort of effect.

Capitanio et al. [4] has recently shown that the subduction rate is controlled by the transformation of potential energy $\dot{E} = \Delta\rho g\dot{r}$ into heat. This dissipation is a function of both the effective viscosity and deformation rate, $D = 1/2 \int \mu\dot{\epsilon}^2$, and is partitioned between the lithosphere and the mantle $(\dot{E}_{\text{sub}} = D_{\text{litho}} + D_{\text{mantle}})$, where the lithospheric viscosity is two to four orders of magnitude higher than the mantle viscosity. As a consequence, the mantle dissipation is caused by the viscous drag exerted by the mantle on the lithosphere, which thus controls the sinking rate [13], while the lithospheric dissipation is rather concentrated at the bending trench. This balance between energy dissipated inside the slab and outside the slab is expected to generate complexities for very wide slabs. We follow a conceptual approach similar to [4], but a completely different numerical approach, in order to obtain some insights into the complexities arising from the presence of the Earth curvature alone.

Most of the geodynamical codes are limited in the geometry (Cartesian box), by the difficulty in handling the sharp change of viscosity at the lithospheric scale (from $O(10^{25}$ Pa s) to $O(10^{20}$ Pa s) within 25 km), in implementing a free surface, and in implementing in one code the very diverse scales involved in subduction (the thickness of the fault at the trench is $O(100$ m)), with the planetary scale $O(10^4$ km) [23]. An ideal numerical approach for solving global geodynamics should be able to reproduce all such diverse components and their effects in a multi-scale framework and in spherical global coordinates. The method that we introduce in this paper is an innovative (Fast Multipole) Accelerated Boundary Element Method (Accelerated-BEM): a tool suitable for studying the largest subduction systems in a spherical setting. In order to avoid confusion, we want to emphasize that this approach is completely different from the one put forward in [23] by the first author of this work where two numerical approaches (finite element and boundary element) were joined. Here a more sophisticated and faster implementation of exclusively the Boundary Element Method, without coupling with any other code, is employed for the first time to analyze the subduction of very large plates, including the Pacific, Nazca, Indian, Farallon, and Thetis plates.

2 Fundamental equations

Most numerical approaches used for modeling geodynamics adopt several assumptions in order to simplify the flow equations to solve, neglecting the effects of elasticity and compressibility. Material properties from laboratory experiments generally convey an effective viscosity $\mu_{\text{eff}}(T,C)$ function of temperature and composition, which compresses the local relationship between stress and strain rate in one number:

$$\sigma = -p\mathbf{I} + 2\mu_{\text{eff}}(T,C)(\nabla\mathbf{u} + \nabla^t\mathbf{u}) = -p\mathbf{I} + 2\mu_{\text{eff}}(T,C)\dot{\epsilon} \tag{1}$$

The Stokes equations comprise the momentum conservation and incompressibility condition

$$\nabla \cdot \sigma + \rho\mathbf{b} = 0 \tag{2}$$

$$\nabla \cdot \mathbf{u} = 0 \tag{3}$$

where $\mathbf{b}$ is the body force vector.

In this paper, we consider how to employ Accelerated-BEM for solving exclusively the Stokes and incompressibility equations. For our problem, this amounts to subdividing the mantle into several closed regions, each characterized by an effective temperature and composition and thus a constant viscosity. When such an approximation is acceptable, it is possible to rewrite (2) and (3) as a boundary integral equation for each subdomain. This constitutes a decrease in the problem dimensionality resulting in potential computational gains. Moreover, this approach offers inherent multiscale capabilities as the surface mesh resolution can vary dynamically to track the physics of interest.

This allows, instead of meshing the entire three dimensional volume $O(L^3)$ (where L is the domain size), in $O(N^3)$ cells of average size D (where $N = L/D$), to mesh each domain in $O(N^2)$ cells, with major computational efficiency gain for very large models. For example, for $N = O(1{,}000)$ one obtains $N^2 = O(10^6) \ll N^3 >= O(10^9)$, and will be more advantageous with increasing computational power. Furthermore this approach allows to mesh the different surfaces with very different resolutions and to refine the zone of interest with a denser number of surfaces.

3 Boundary formulation of Stokes fluids interfaces

3.1 Boundary equations

We consider Stokes flow as described by (2) and (3). Assuming a constant μ in each domain, the velocity of each point inside the domain can be written as a sum of two surface integrals [25], called single and double layer integrals, respectively, representing the effects of the forcing $\sigma_{ik}(\mathbf{x})\, n_k$ and velocity $u_i(\mathbf{x})$

$$-\frac{1}{8\pi\mu}\int_{\partial D}\sigma_{jk}(\mathbf{x})n_k G_{ij}(\mathbf{x},\mathbf{x}_o)\mathrm{d}S(\mathbf{x}) + \frac{1}{8\pi}\int_{\partial D}u_j(\mathbf{x})n_k T_{ijk}(\mathbf{x},\mathbf{x}_o)\mathrm{d}S(\mathbf{x}) = \begin{cases} u_i(\mathbf{x}_o) & \text{if } \mathbf{x}_o \in D, \\ 0 & \text{otherwise} \end{cases} \tag{4}$$

where G_{ij} and T_{ijk} are the steady Green's functions for velocity and stress respectively, also known as the *Stokeslet* and the *Stresslet*

$$G_{ij}(\mathbf{x}-\mathbf{x}_o) = \frac{\delta_{ij}}{r} + \frac{\hat{x}_i\hat{x}_j}{r^3};\ \hat{\mathbf{x}} = \mathbf{x}-\mathbf{x}_o \text{ and } r = |\hat{\mathbf{x}}| \tag{5}$$

$$T_{ijk}(\mathbf{x}-\mathbf{x}_o) = -6\frac{\hat{x}_i\hat{x}_j\hat{x}_k}{r^5}. \tag{6}$$

3.2 Simple formulation with N "democratic" layers

Let us consider N domains as in Fig. 1, each of which is defined by a density ρ_i and viscosity μ_i. The approach is called "democratic" because it is assumed that all domains are embedded in a background fluid of density ρ_o and viscosity μ_o, as in the approach of [21, 25]. As a consequence, the relative material properties are defined as: $\Delta\rho_i = \rho_i - \rho_o$ and $\lambda_i = \mu_i/\mu_0$. If the only active force is gravitational buoyancy, the jump at the interface can be written as $\Delta\mathbf{f} = \Delta\rho(\mathbf{b}\cdot\mathbf{x})\cdot\mathbf{n}$.

We follow here the approach of Pozrikidis [25], which recalls the original formulation of [41]. Equation (4) yields for the velocity inside each domain D_i

$$\mathbf{u}(\mathbf{x}_o) = -\frac{1}{8\pi\mu_i}\int_{\partial D_i}\Delta\mathbf{f}\cdot\mathsf{G}(\mathbf{x},\mathbf{x}_o)\cdot\mathbf{n}\,\mathrm{d}S(\mathbf{x}) + \frac{1-\lambda_i}{8\pi}\int_{\partial D_i}\mathbf{u}(\mathbf{x})\cdot\mathsf{T}(\mathbf{x},\mathbf{x}_o)\cdot\mathbf{n}\,\mathrm{d}S(\mathbf{x}) \tag{7}$$

while the velocity in the background outside all the domains D_i can be written using a symmetrical formulation

$$\mathbf{u}(\mathbf{x}_o) = -\frac{1}{8\pi\mu_i\lambda_i}\int_{\cup\partial D_i}\Delta\mathbf{f}\cdot\mathsf{G}(\mathbf{x},\mathbf{x}_o)\cdot\mathbf{n}\,\mathrm{d}S(\mathbf{x}) + \frac{1-\lambda_i}{8\pi\lambda_i}\int_{\cup\partial D_i}\mathbf{u}(\mathbf{x})\cdot\mathsf{T}(\mathbf{x},\mathbf{x}_o)\cdot\mathbf{n}\,\mathrm{d}S(\mathbf{x}) \tag{8}$$

If we let the point $\mathbf{x}_o$ converge to the boundary and consider the principal value (PV) for diverging terms (T), we obtain the velocity at the interface

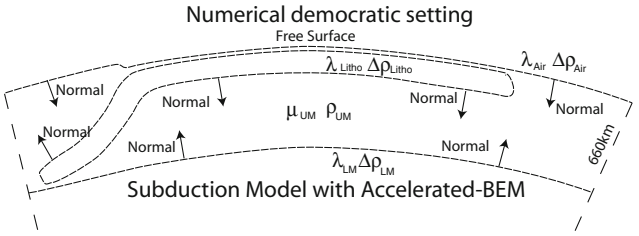

Fig. 1 Structure of the Accelerated Boundary Element Method applied to a subduction problem. A "democratic" structure of the boundaries is employed, requiring the solution of a distinct set of equations described in Sect. 3. "Democratic" stands for the fact that all surfaces bound a same background domain. This is indicated by the arrows "Normal", all directing toward the upper mantle, the background domain in the setup employed in this work. The numerical solution requires the absolute density and viscosity of the upper mantle and the relative densities and viscosities of the other domains, defined as differential densities and viscosity ratios through the surfaces (i.e. Earth surface, Lithosphere and upper-lower mantle transition in the present setup). A very thin layer divides the Earth surface from the lithosphere; the numerical treatment of these contacting surfaces is described in the text. The "democratic" setting allows a great simplification of the equations to solve compared to a general one

$$\frac{1+\lambda_i}{2}\mathbf{u}(\mathbf{x}) = \sum_j^N \frac{1-\lambda_j}{8\pi}\int_{\partial D_j}^{\mathrm{PV}}\mathbf{n}\cdot\mathsf{T}\cdot\mathbf{u}\,\mathrm{d}S - \frac{1}{8\pi\mu_0}\sum_j^N\int_{\partial D_j}\mathsf{G}\cdot\Delta\mathbf{f}\,\mathrm{d}S\,, \tag{9}$$

which can be discretized in boundary elements (also called Panels).

3.3 Numerical method

The surfaces S_i in Fig. 1 and the supported quantities $\mathbf{u}$, $\Delta\mathbf{f}$,… are discretized with boundary elements (or panels). The boundary integral Equation 5, thus becomes a linear system

$$((1+\lambda)/2 + \mathsf{T})\mathbf{U} = \mathbf{F}. \tag{10}$$

Many approaches carry out the construction of the matrix; this scales as N^2_{panels} both memory- and computation time-wise though, making it impractical for large systems.

We use a Fast Multipole Method (Accelerated BEM) [1, 14, 40] for the evaluation of the integrals in (5). The Accelerated algorithm scales as $N\log(N)$, which is far more tractable and still allows the use of a Generalized Minimized Residual Method (GMRES) or any Krylov space-based method that does not rely on the storage of the full matrix.

A multipole method exploits the decay of the kernel to convolve and makes a controlled approximation. More explicitly, let us compute

$$u(\mathbf{x}_o) = \int_D G(\mathbf{x}_o - \mathbf{x})\rho(\mathbf{x})\mathrm{d}V(\mathbf{x}). \tag{11}$$

We consider the contribution from D_i, a part of D that is far *enough* from our evaluation point $\mathbf{x}_o$, and proceed with a Taylor expansion of the kernel G about $\mathbf{x}_c \in D_i$

$$\begin{aligned} u(\mathbf{x}_o) &= \int_{D_i} G(\mathbf{x}_o - \mathbf{x})\rho(\mathbf{x})\mathrm{d}V(\mathbf{x}) \\ &\simeq \int_{D_i} (G(\mathbf{x}_o - \mathbf{x}_c) - \nabla G(\mathbf{x}_o - \mathbf{x}_c)\cdot(\mathbf{x}_o - \mathbf{x}_c) + \cdots) \\ &\quad \rho(\mathbf{x})\mathrm{d}V(\mathbf{x}) \\ &\simeq G(\mathbf{x}_o - \mathbf{x}_c)\int_{D_i} \rho(\mathbf{x})\mathrm{d}V(\mathbf{x}) \\ &\quad - \nabla G(\mathbf{x}_o - \mathbf{x}_c)\cdot\int_{D_i} (\mathbf{x}_o - \mathbf{x}_c)\rho(\mathbf{x})\mathrm{d}V(\mathbf{x}) + \cdots \end{aligned} \tag{12}$$

We note that the equation involves successive moments of the ρ distribution in D_i . The accelerated algorithm thus sorts the sources in a tree structure whose cells contain the moment integrals—or multipoles—and carries out a field evaluation through a tree traversal. The refinement of the interactions is determined by a tree traversal stopping criterion based on a prescribed tolerance. The reader is referred to [1, 14, 40] for general information on multipole methods and the work of Tornberg and Greengard [37] for the transposition of harmonic multipoles to the evaluation of the Stokeslet and Stresslet. The present accelerated code can handle convolutions with the Green's functions for the Poisson equation, the Stokeslet or the Stresslet. It employs up to the second order moments of the source distributions (quadrupoles).

3.4 Performance

The Fast Multipole algorithm drastically improves the computational cost of the Boundary Element Method. Figure 2 shows the computation time of a time step for a viscous sphere under gravity for several tolerances and resolutions. For the coarse resolutions, the method displays the nominal N^2 scaling of a direct interaction code. This is attributed to the relatively few elements and tree cells. The scaling then quickly approaches a nearly linear one (N log(N)) for the finer resolutions.

The Accelerated-BEM has been parallelized using MPI. Figure 3 shows the parallel efficiency tested on a Opteron cluster with Quadrics connections. The scaling is very good up to 64 CPUs, still keeping 90% efficiency. In its current implementation, the Accelerated-BEM uses a shared tree, thus reducing the communication load at the expense of memory requirements.

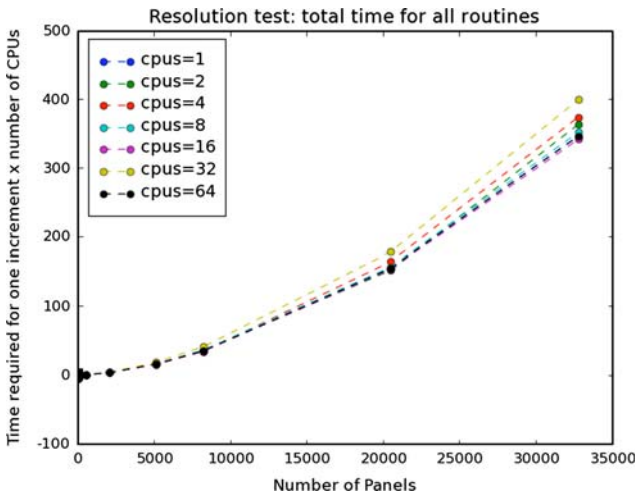

Fig. 2 Fast Multipole Boundary Element Method: resolution test for 10 to 10^5 panels (=boundary elements). The execution time of one time step is re-normalized through the multiplication for the number of CPUs. The scaling begins quadratically and becomes linear for large problems. The time step embeds the entire parallelized massive parallel processing (MPP) and non parallelized (client) process

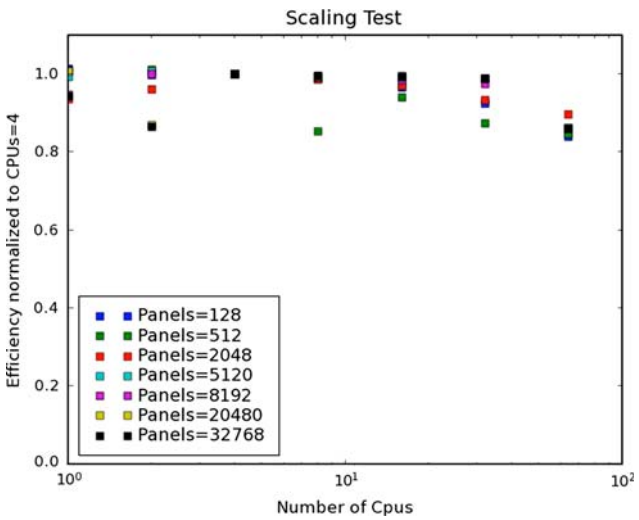

Fig. 3 Fast Multipole Boundary Element Method: efficiency of the parallelization implementation, tested for 1–64 processors. The execution time of one time step is re-normalized using the results of 4 CPUs in order to avoid effects due to the use of dual machines as nodes. The time step embeds the entire parallelized (MPP) and non-parallelized (client) process

3.5 Time evolution

The solver employs a smoothed explicit scheme: $x_{t+\Delta t} = x_t + \frac{1}{2}(v_t + v_{t-\Delta t})\Delta t$. The system (10) has some degenerate eigenvalues, which correspond to the rigid translation and rotation of the whole problem: their eigenmodes are numerically inhibited. Additionally, the conservation of mass/volume can be affected by a numerical drift,

corresponding to all the spherical eigenmodes, which are handled with additional constraints and damping.

The model then requires about 20 increments to stabilize and damp the first modes while the whole simulation performs in about 400 increments. An alternative approach for inhibiting the eigenmodes is to use an iterative implicit solver of the form $x_{t+\Delta t} = x_t + \frac{1}{2}(v_{t+\Delta t} + v_t)\Delta t$, now in a testing phase.

3.6 Contact algorithm

During the evolution of the system the surfaces can enter in contact. An adaptive mesh algorithm has been implemented in order to avoid that surfaces could cross each other. The contact algorithm checks that the surfaces cannot be closer then a certain critical distance h_{crit}. The actual implementation requires a predefined Master–Slave hierarchy between the surfaces. At each time step the nodes of the Slave surface that are close to the critical distance are displaced at the critical distance itself (distances are all defined at the closest element of the master surface). In all the models proposed in this paper, the slave surface is chosen as the one that confines with the lowest viscosity. Typically, the critical distance is chosen equal to one third of the size of the contact elements. If the distance is too low, instabilities arise during the computation and if it is too high the contact between the two surfaces is not properly calculated. The parallelization of the contact algorithm is still a work in progress. With the actual implementation the time required for the contact is so small compared to the rest that it is not yet a priority, but in light of a massive parallel implementation this should be done.

4 Modeling subduction with accelerated-BEM setting

Subduction is the process through which a highly viscous ($O(10^2)\mu_{\text{UM}}$) and heavy plate (1–3% of viscosity increase) enters into the Earth. Laboratory and numerical models [5, 10, 12, 15, 16, 18, 19, 29, 31] have shown that the process is mainly controlled by the interaction of the lithosphere with the surface and is one-sided, characterized by an unsubducted plate overlapping the subducting plate. Seismic tomography and Benioff Zone studies have shown that they penetrate down into the mantle assuming complex shapes [6, 11, 17, 38, 39]. We assume that three fundamental forces control the subduction process: the lithosphere–mantle–air/water buoyancy difference, the viscous resistance of the mantle to the plate motion and the resistance to bending and stretching of the lithosphere itself.

Buoyancy difference arises from the density difference between the bottom and the top of the plate, of the mantle and air/water, respectively. This property is critical in subduction as it prevents the unsubducted plate from sinking straight down [12]. The contact algorithm described in the prior section takes care of this effect, as the contact algorithm automatically adapts the free-surface to the lithospheric topography, generating a physically consistent Archimedes force. The radial displacement due to the movements of the free surface compares well with the expected isostatic equilibrium, as below an 80-km thick lithosphere 3 km of subsidence are obtained as model results.

The resistance to bending and stretching of the lithosphere itself is controlled by its very diverse and complex inner rheology. Simplified models of the internal distribution of strength of an oceanic lithosphere display a peak at 30–40 km depth, where all the strength of the lithosphere is stored [4, 27, 28]. In this work, the overall resistance to bending and stretching is parameterized by an effective uniform layer with a viscosity two orders of magnitude higher than that of the mantle.

BEM solvers work equally well with uniform and non-uniform mesh. In order to profit from this property, a better refined mesh is imposed around the region where the plate subducts at the beginning of the simulation. The implementation of subduction at the global scale in a uniform Earth is obtained using only three surfaces, one delimiting the Earth surface, the second the lithosphere–mantle boundary and the third the boundary between an upper less viscous mantle and a lower 30 times more viscous mantle. We use the democratic boundary integral formulation (9) sketched in Fig. 1.

The reference viscosity μ_0 of Eq. 9 is the upper mantle effective viscosity μ_{UM}; $\lambda_1 = \mu_{\text{Ocean}}/\mu_{\text{UM}}$ is virtually null, being the ratio between the viscosities of ocean (water) and the upper mantle; $\lambda_2 = \mu_{\text{Litho}}/\mu_{\text{UM}}$ is the ratio between the lithosphere and upper mantle viscosities; $\lambda_3 = \mu_{\text{LM}}/\mu_{\text{UM}}$ is the ratio between the lower and upper mantle viscosities. We define $\Delta\mathbf{f}$ on surfaces 1, 2 and 3 in the same fashion; they are equal to the difference between ocean (water) and upper mantle densities, the difference between the lithosphere and upper mantle densities and the difference between lower and upper mantle densities

$$\Delta\mathbf{f}_1 = (\rho_{\text{Ocean}} - \rho_{\text{UM}})gr\,\mathbf{n}$$

$$\Delta\mathbf{f}_2 = (\rho_{\text{Litho}} - \rho_{\text{UM}})gr\,\mathbf{n}$$

$$\Delta\mathbf{f}_3 = (\rho_{\text{LM}} - \rho_{\text{UM}})gr\,\mathbf{n}$$

where r is the length of $\mathbf{x}$, g is the gravity acceleration ($10\ m^2/s$) and gravity is assumed constant and radial $\mathbf{b} = -g\ \mathbf{x}/r$.

The solution of Eq. 9 with the parameters described above is shown in Fig. 4. The plots illustrate the simulation of subduction of a large plate, (6,000 km × 6,000 km), 80 km thick, with a mantle 3,000 km thick. In order to avoid the complications that are displayed in the next

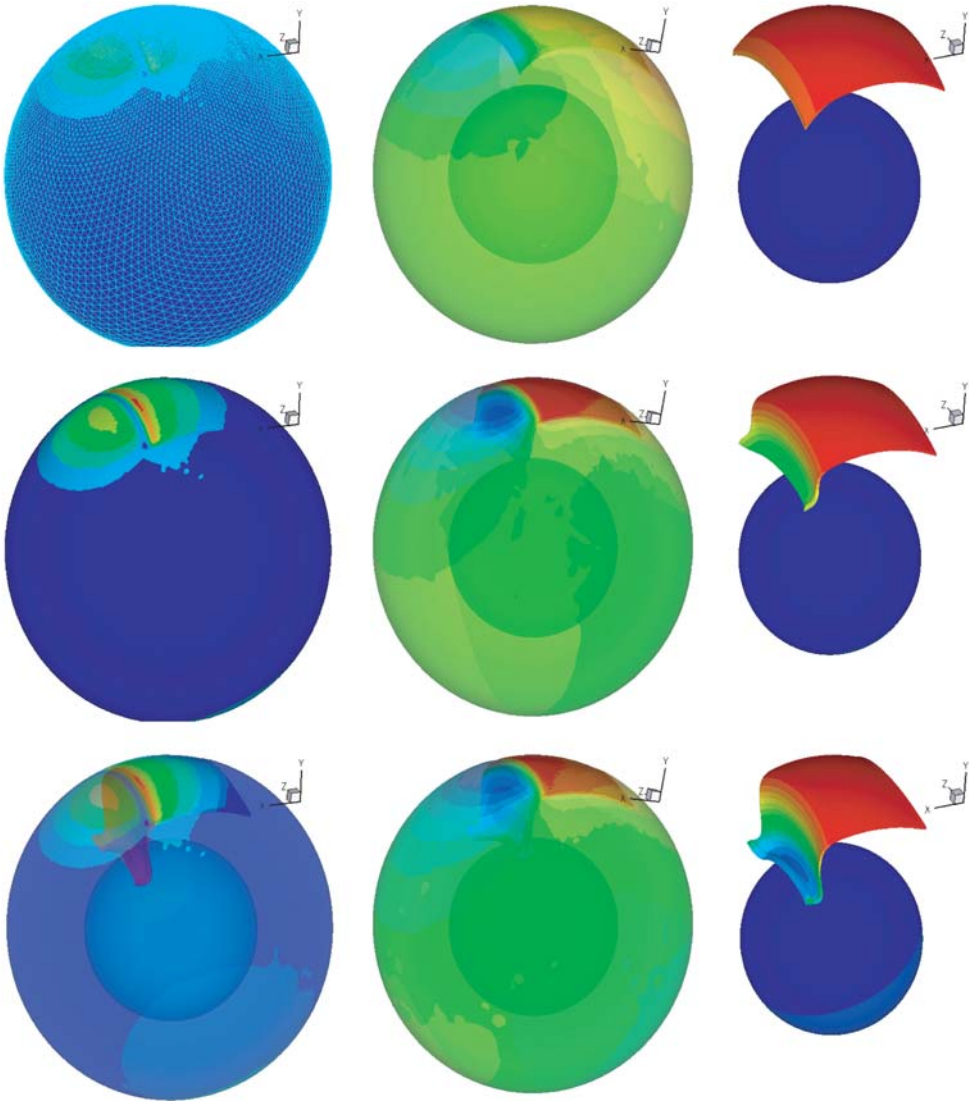

Fig. 4 Illustration of a simulation of subduction in spherical coordinates obtained with the Accelerated-BEM. In this example, a 6,000 km × 6,000 km slab of 80 km thickness is subducting down to a viscosity discontinuity of 30 times at 3,000 km depth. The three panels on the right show, respectively, the mesh of the external surface, highly resolved around the subducting slab and the radial absolute velocity at the surface and inside (through a transparent plot). The radial velocity is higher at the trench where it sinks faster, and has a second peak (but with opposite sign) at the wedge. The three panels on the center show the evolution of the slab from the initial configuration to the final in a transparent plot, and the color represent the horizontal velocity. Finally, the last set of figures shows the slab evolution of the same simulation, without plotting the external surface. Colors in this case represent the radial coordinate

section, the plate boundary is "cut" in a Cartesian square, so the trench is initially already concave and it remains concave for all the simulations. The plots of Fig. 4 show how the trench is automatically emerging out of the model setup, where the plate sinks faster and an upwelling arises in front of the trench, displacing the mantle in a broad region. Test on the free surface show an equivalent depression of 3 km over the oceanic plate, as predicted by isostatic equilibrium. The evolution of subdction shows a non-trivial partitioning between plate sinking, trench retreat and plate advance, which needs further investigation.

5 Role of Earth curvature on the subduction of very wide plates

5.1 Setup

In Fig. 4 the slab morphology is very simple, accommodating the reduced space available with depth with a uniform bending. In this section, we propose several models with a wide plate ($W = 6{,}000$ km and $W = 9{,}000$ km) and a transition to a highly viscous mantle at a predefined depth. Differently from the above illustrative example, the initial

plate boundaries are chosen all along the main circles, so the plate extends farther at its center, where the width is measured. In order to study the role of Earth curvature, we compare two fundamental models: "Earth-like" (radius = ER = 6,371 km) and "flat Earth" (radius = 2ER = 12,742 km). Figure 5 illustrates the two setups for the plate 9,000 km wide. All other physical properties are imposed identically for the two models and are displayed in Table 1.

The viscosity jump at 1,600 km depth has been chosen to correspond to most lower mantle viscosity models. The resolution for the lithosphere is 50 km in the horizontal directions and 40 km in the radial direction, requiring a total of about 40 k boundary elements. The external surface and the mantle transition surfaces are composed of 20,000 boundary elements each, highly refined over the subducting plate, as in the analogue case shown in Fig. 4.

5.2 Results and discussion

During the simulation the trench migrates at a much smaller velocity than the subduction rate, while it reorganizes its shape. The upper panels of Fig. 6 show the view from the top of the planetary surface when about 2/3 of the plate is subducted (2,000 of 3,000 of plate length) for the widest tested plate ($W = 9{,}000$ km). Colors show the surface velocity V_x, with different saturation for the two models. In the "flat Earth" case the distributed background velocity is spread on a larger area, while in the Earth-like model the back flow and the area dragged by the moving plate are more localized. In all cases the plate advances faster in the center and produces a corner flow of a size proportional to the trench width. In front of the trenches the backflow velocity displays two peaks close to the slab edge, but on the "flat Earth" case they are isolated and the backflow deformation is distributed, while for the "Earth-like" model the peaks are less pronounced and the back-arc flow is more uniform.

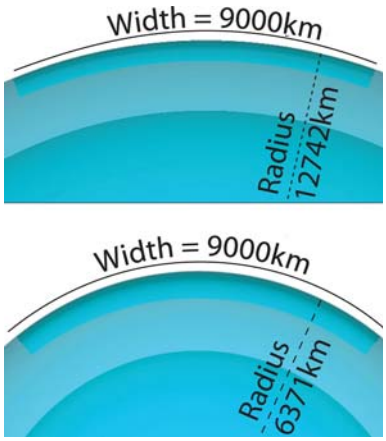

Fig. 5 Initial setup of subduction for the "Earth-like" (*top*) and "flat Earth" (*bottom*) cases for a plate of width $W = 9{,}000$ km. The case of a plate with $W = 6{,}000$ km is analogous. The initial plate boundaries are chosen all along the main circles so that the plate is widest at its center, where the width is measured

Table 1 Common assumption for the "flat Earth" and "Earth-like" cases

Physical entity	Characteristic	Quantity
Lithosphere	Thickness	80 km
Lithosphere	Length	3,000 km
Lithosphere	Width	6–9,000 km
Lithosphere mantle	Viscosity ratio	200
Deep mantle discontinuity	Depth	1,600 km
Deep mantle discontinuity	Viscosity ratio	30
Atmosphere mantle	Viscosity ratio	0.1
Atmosphere	Density	0.0
Lithosphere	Density	1.3
Upper mantle	Density	1.0
Deep mantle	Density	1.03

The bottom panels of Fig. 6 show the same model, illustrating the boundaries below the Earth surface: the subducting lithosphere and the inner mantle discontinuity appear. The two models once again look similar, except the curvature which is slightly higher for the plate on the Earth-like setting. Furthermore, a closer look at the edges displays a distinct "hook" shape for the "flat Earth" model, as predicted also by [23], however in the "Earth-like" model the "hook" is less pronounced. Our models, therefore, confirm that the trench of a very wide uniformly viscous plate will tend to show as a first approximation an "S" shape, as suggested in [32]. However, in the "Earth-like" setting the shape of the "S" tends to be dominated by the large convex curvature and plate advance, while the concave curvature of the edges is smaller.

The main characteristics of the "Earth-like" model appear in the developed deep morphology, plotted in Fig. 9. While in the "flat Earth" case, the slab shape close to the edges is dominated by the "hook" shape (Fig. 7) and numerous small undulations appear in the slab center, in the "Earth-like" model, together with the edge "hook" shape, a more distinct folding process appears toward the center of the slab (Fig. 9). Also the increase of the folding amplitude with depth is coherent with the postulated role of earth curvature and lack of space in inducing the inner plate folding. The wavelength arising in the "Earth-like" model for the dominant undulations (1,000–2,000 km) is also consistent with a simple stability analysis for viscous folding in an infinite matrix gives an expected wavelength $L = 2\pi h\left(\frac{\mu_l}{6\mu_m}\right)^{1/3}$, which corresponds to a value of 1,600 km. The two initial model setups "flat Earth" and "Earth-like" are equal under any other aspect, implying

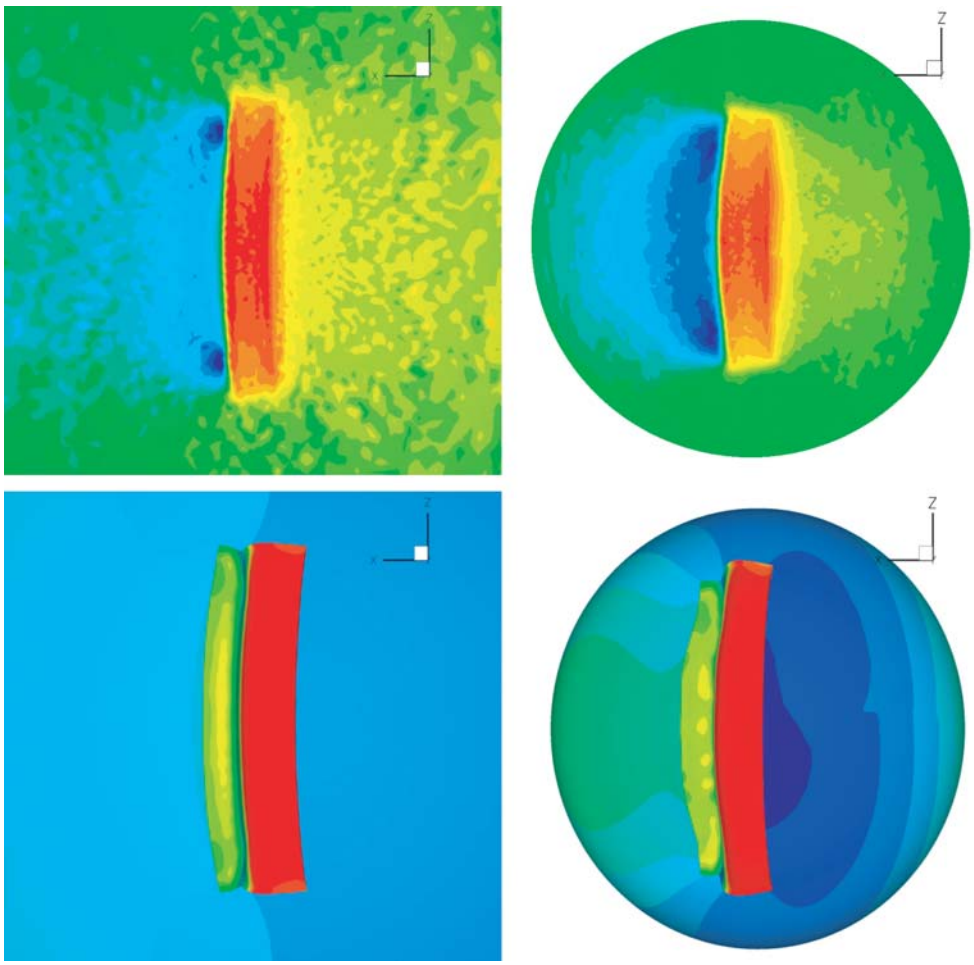

Fig. 6 Top view of the plates for a "flat Earth" (*left*) and for an "Earth-like" (*right*) for the plate 9,000 km wide. In the *top panels*, the colors represent the velocity in the *X* direction on the planetary surface, after the plate has subducted by about 2/3 of its length. On the *bottom panels* the "look inside" of the same model is proposed, as the Earth surface is not anymore displayed and only the slab and the deep mantle discontinuity (1,600 km depth) are plotted using the same color diagram

that the shown effect is clearly due to the restricted space that the plate has when sinking into the mantle, which creates a background stress that the plates accommodate in a different manner.

The wavelength of the fold is of the order O(1,000 km), much larger than the model resolution (50 km), as displayed in Fig. 8, where the final stage of two runs of the same model (9000 km wide plate subducting in a "Earth-like" setting) are displayed. The left and right panels differ only for length of the explicit time step chosen during the simulation. The model on the left underwent a bifurcation characterized by the splitting of one fold of the inner plate, while the result obtained by the model on the right, characterized by a finer time stepping, maintained its symmetry. The morphology of this best model (same as panel B of Fig. 7) is illustrated in detail through sections at regular depths in Fig. 8. In general, however, irrespective of the numerical oscillations encountered, in all the models that we tested we observed the dual behavior characterized by concave edges and complexities in the center of the plates, with wavelength coherent with the above analysis of the fold length. This result shows the importance of Earth curvature in shaping the deep morphology of very wide plates. However, further analysis and parameter searches are necessary to assess the exact role played by and Earth-like versus Cartesian setting.

6 Conclusions

Fast multipole acceleration of the boundary element method has been applied for the first time as a computational approach suitable for modeling plate tectonics. The code scales linearly with the problem size for large sizes (more than 10^3 elements) and shows a very good parallel behavior that is promising for larger systems. An adaptive mesh algorithm has been developed for reproducing the buoyancy force, within a free surface setting. Exploiting

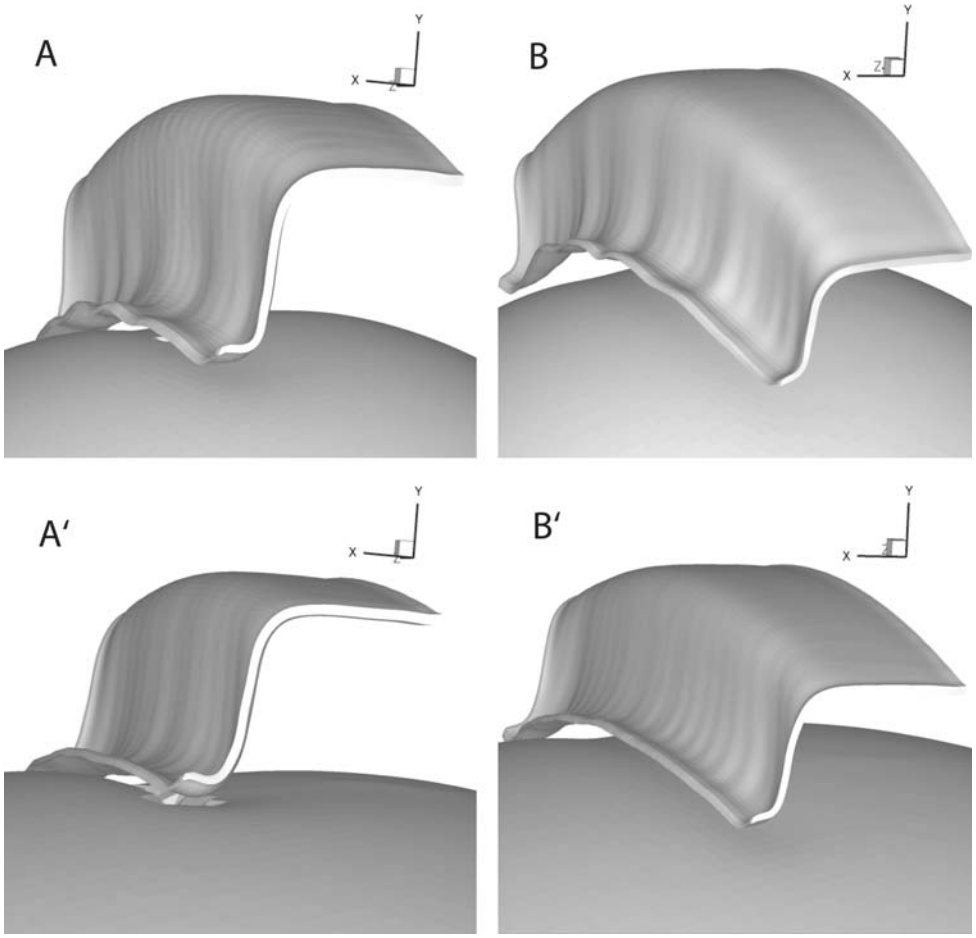

Fig. 7 Slab morphology for "Earth-like" (*top*) compared to the one of "flat Earth" (*bottom*) for two plates, one 6,000 km wide (**a** and **a**′) and one 9,000 km wide (**b** and **b**′). In both cases, a dual behavior is characterized by a concave curvature at the sides and a complex folding in the center. The B model has been tested for different time steps (see Fig. 2) and detailed sections of its morphology are displayed in Fig. 2

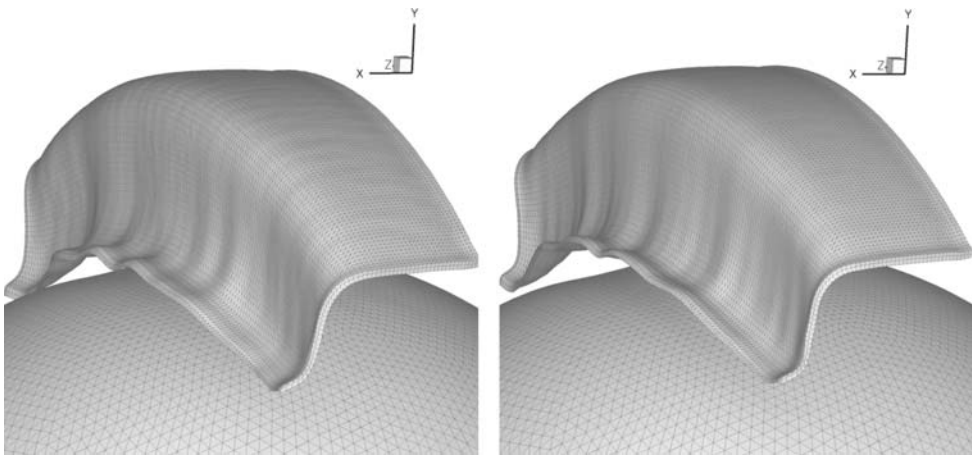

Fig. 8 Two runs of the same "Earth-like" for a plate 9,000 km wide employing a different explicit time step. In the *right panel*, the result is shown with a finer time step. The mesh is displayed for both examples: the resolution 50 km is much finer for the complex undulations. The model on the left panel shows some asymmetries, while the one on the right is almost perfectly symmetric and its detailed morphology is displayed in Fig. 2

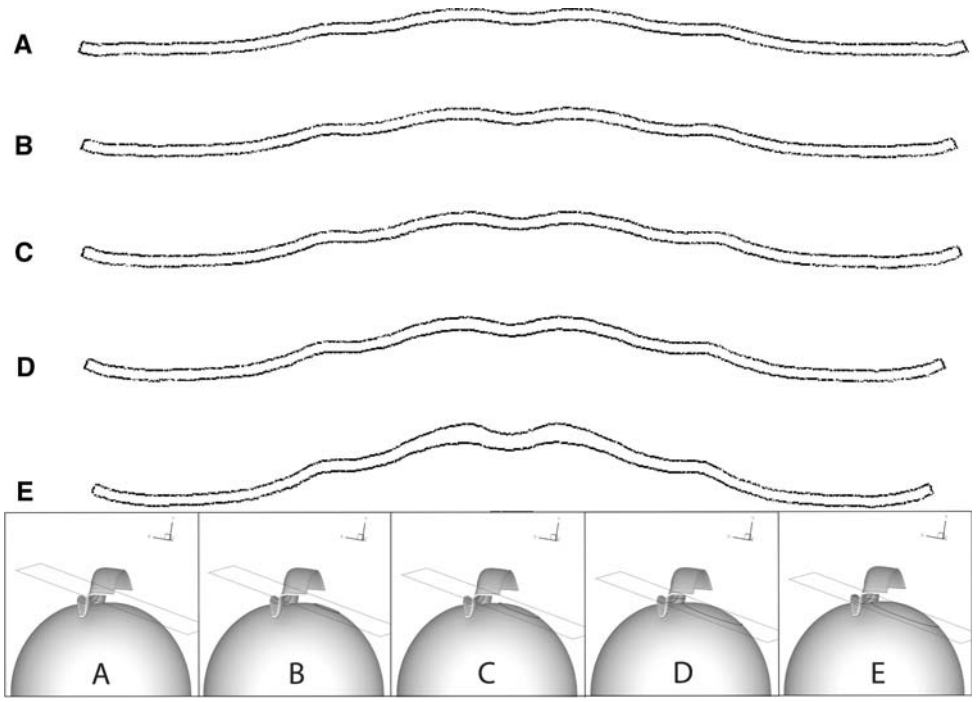

Fig. 9 Slides of the "Earth-like" model taken at regular distance for the finest model (**b** of Fig. 2). The solution is symmetric and the development of the the dual behavior (concave curvature at the edges and complexities in the plate center) is present through the entire subducted slab although the complexities amplitude increases with depth

this innovation, for the first time Accelerated-BEM has been employed for modeling subduction at the planetary scale. An illustrative example has been presented for subduction in a viscously uniform Earth and in an Earth with 3,000 km thick uniform mantle.

Our models support the idea that Earth curvature can have an important role during the subduction of very wide plates. Such plates present a lateral hook shape due to feedback with mantle flow [12, 23], an inhibited trench retreat [35] and consequent surface pattern as an *S* shape [32]. It has also been already proposed through the comparison with analogue experiments how the slabs beneath the transition zone might buckle [30]. We find that Earth curvature contributes to slab morphology in an important manner, modifying the shape of the subducted slab, which develops a folding structure in the centre of the slab and more pronounced at depth. This bimodal slab pattern in one subduction system (edge at the site, complex folding in the centre) has not been observed in prior numerical models.

A comparison with nature offers also interesting insights. The longest trenches on the Earth are all segmented. The length of most of the arcs in which the Pacific trench is divided is in the range 1,000−2,000 km. Our results suggest that large slabs present more complexities in its center compared to its edges. This might be a more general concept, enabling us to speculate on some of the complexities observed for the widest plates. The slabs of Pacific and Nazca plates could indeed amplify the folding event in the center of the trench, namely in the center of the South-American (Peru–Bolivia) in the East side and in the center of the West Pacific trench, namely Izu–Bonin–Mariana and Japan subduction systems. In the past, at the center of the Thetis plate a similar effect might have also been visible.

Acknowledgments This work, as part of the Eurohorcs/ESF European Young Investigators Awards Scheme, was supported by funds from the National Research Council of Italy and other National Funding Agencies participating in the 3rd Memorandum of Understanding, as well as from the EC Sixth Framework Programme.

References

1. Barnes J, Hut P (1986) A hierarchical O(N log N) force-calculation algorithm. Nature 324
2. Bird P (2003) An updated digital model of plate boundaries. Geochem Geophys Geosyst 4(3):1027. doi:10.1029/2001GC000252
3. Carlson RL, Hilde TWC, Uyeda S (1983) The driving mechanism of plate tectonics: relation to age of the lithosphere at trenches. Geophys Res Lett 10:297–300
4. Capitanio FA, Morra G, Goes S (2007) Dynamic models of downgoing plate buoyancy driven subduction: subduction motions and energy dissipation. Earth Planet Sci Lett (in press)
5. Christensen UR (1996) The influence of trench migration on slab penetration into the lower mantle. Earth Planet Sci Lett 140:27–39
6. Cizkova H, Cadek O, Van den Berg AP, Vlaar NJ (1999) Can lower mantle slab-like seismic anomalies be explained by thermal

coupling between upper and lower mantles? Geophys Res Lett 26:1501–1504
7. Davies G (1980) Thermal histories of convective Earth models and constraints on radiogenic heat production in the Earth. J Geophys Res 85:2517–2530
8. Davaille A, Jaupart C (1993) Transient high-Rayleigh-number thermal convection with large viscosity variations. J Fluid Mech 253
9. Davaille A, Jaupart C (1994) Onset of thermal convection in fluids with temperature-dependent viscosity: application to the oceanic mantle. J Geophys Res 99:19,853–19,866
10. Faccenna C, Davy P, Brun JP, Funiciello R, Giardini D, Mattei M, Nalpas T (1996) The dynamics of back-arc extension: an experimental approach to the opening of the Tyrrhenian Sea. Geophys J Int 126(3):781–795
11. Fukao Y, Widiyantoro S, Obayashi M (2001) Stagnant slabs in the upper and lower mantle transition zone. Rev Geophys 39:291–323
12. Funiciello F, Morra G, Regenauer-Lieb K, Giardini D (2003) Dynamics of retreating slabs (part 1): insights from 2-D numerical experiments. J Geophys Res 108(B4):2206. doi:10.1029/2001JB000898
13. Goes S, Capitanio FA, Morra G (2008) Evidence of lower mantle slab penetration phases in plate motions. Nature (in press)
14. Greengard L, Rokhlin V (1987) A fast algorithm for particle simulations. J Comput Phys A 73:325–348
15. Gurnis M, Hager BH (1988) Controls of the structure of subducted slabs. Nature 335:317–321
16. Guillou-Frottier L, Buttles J, Olson P (1995) Laboratory experiments on the structure of subducted lithosphere. Earth Planet Sci Lett 133:19–35
17. Isacks B, Molnar P (1971) Distribution of stresses in the descending lithosphere from a global survey of focal mechanism solutions of mantle earthquakes. Rev Geophys 9:103–174
18. Ita J, King SD (1998) The influence of thermodynamic formulation on simulations of subduction zone geometry and history. Geophys Res Lett 25:1463–1466
19. Jacoby WR (1973) Model experiment of plate movements. Nat Phys Sci 242(122):130–134
20. Lallemand S, Heuret A, Boutelier D (2005) On the relationships between slab dip, back-arc stress, upper plate absolute motion, and crustal nature in subduction zones. Geochem Geophys Geosyst 6:917
21. Manga M, Stone HA (1995) Low Reynolds number motion of bubbles, drops and rigid spheres through fluid-fluid interfaces. J Fluid Mech 287:279–298
22. Moresi L, Gurnis M (1996) Constraints on the lateral strength of slabs from three-dimensional dynamic flow models. Earth Planet Sci Lett 138:15–28
23. Morra G, Regenauer-Lieb K (2006) A coupled solid–fluid method for modeling subduction. Phil Mag 86:3307–3323
24. Morra G, Regenauer-Lieb K, Giardini D (2006) Curvature of oceanic arcs. Geology 34:877–880
25. Pozrikidis C (1992) Boundary integral and singularity methods for linearized viscous flow
26. Phillips BR, Bunge H-P (2005) Heterogeneity and time dependence in 3D spherical mantle convection models with continental drift. Earth Planet Sci Lett 233:121–135
27. Regenauer-Lieb K, Yuen DA (2003) Modeling shear zones in geological and planetary sciences: solid- and fluid-thermal-mechanical approaches. Earth Sci Rev 63:295–349
28. Regenauer-Lieb K, Yuen D, Branlund J (2001) The initiation of subduction: criticality by addition of water? Science 294:578–580
29. Ricard Y, Richards MA, Lithgow-Bertelloni C, Lestunff Y (1993) Geodynamic model of mantle density heterogeneity. J Geophys Res 98:21895–21909
30. Ribe NM, Stutzmann E, Ren Y, van der Hilst R (2007) Buckling instabilities of subducted lithosphere beneath the transition zone. Earth Planet Sci Lett 254:173–179
31. Royden LH, Husson L (2006) Trench motion, slab geometry and viscous stresses in subduction systems. Geophys J Int 167:881–905
32. Schellart WP, Freeman J, Stegman DR, Moresi L, May D (2007) Evolution and diversity of subduction zones controlled by slab width. Nature 446. doi:10.1038/nature05615
33. Sdrolias M, Mueller RD (2006) Controls on back-arc basin formation. Geochem Geophys Geosyst 7. doi:10.1029/2005GC001090
34. Sornette D, Pisarenko V (2003) Fractal plate tectonics. Geophys Res Lett 30(3):1105. doi:10.1029/2002GL015043
35. Stegman DR, Freeman J, Schellart WP, Moresi L, May D (2006) Influence of trench width on subduction hinge retreat rates in 3-D models of slab rollback. Geoc Geophy Geosys 7:1–22
36. Tackley P (2000) Self-consistent generation of tectonic plates in time- dependent, three-dimensional mantle convection simulations, 1. Pseudoplastic yielding. Geochem Geophys Geosyst 1:23
37. Tornberg AK, Greengard L (2007) A fast multipole method for the three dimensional stokes equations. J Comput Phys (in press)
38. Van der Hilst RD, Karason H (1999) Compositional heterogeneity in the bottom 1000 kilometers of Earth's mantle: toward a hybrid convection model. Science 283(5409):1885–1888
39. Van der Voo R, Spakman W, Bijwaard H (1999) Mesozoic subducted slabs under Siberia. Nature 397:246–249
40. Warren MS, Salmon JK (1993) A parallel hashed Oct-Tree N-body algorithm. In: Supercomputing, FMM93, pp 12–21
41. Youngren GK, Acrivos A (1975) Stokes flow part a particle of arbitrary shape: a numerical method of solution. J Fluid Mech 69(2):377–403
42. Zhong S, Gurnis M (1995) Mantle convection with plates and mobile, faulted plate margins. Science 267:838–843